Comparative Analysis of Control Strategies for Large Doubly-Fed Reluctance Wind Generators

Sul Ademi, Milutin Jovanović and Jude K. Obichere

Abstract—This paper deals with field-oriented control (FOC) and vector control (VC) of a promising brushless doubly-fed reluctance generator (BDFRG) technology for large-scale wind turbines. The BDFRG has been receiving increasing attention because of the low operation & maintenance costs afforded by the use of partially-rated power electronics, and the high reliability of brushless construction, while offering performance competitive to its well-known slip-ring counterpart, the doubly-fed induction generator (DFIG). The two robust control schemes have been developed for a custom-designed BDFRG fed from a conventional 'back-to-back' IGBT converter. The preliminary studies have evaluated and compared the algorithms under the maximum torque per inverter ampere (MTPIA) conditions allowing the improved efficiency of the generator-converter set and the entire wind energy conversion system (WECS).

Index Terms—Wind Power, Brushless, Doubly-Fed Machines, Vector Control.

I. Introduction

THE brushless doubly-fed generator (BDFG) has been considered as a viable alternative to the traditional DFIG for wind turbines [1]–[7]. In these applications, where only a limited variable speed capability is required (e.g. typically, in a 2:1 range or so [1], [4], [8]), the BDFG should retain the DFIG economic benefits of using a relatively smaller inverter (e.g. around 25% of the machine rating), but with higher reliability and maintenance-free operation by the absence of brush gear [9], [10].

The BDFG has two standard stator windings of different applied frequencies and pole numbers, unlike the DFIG. The primary (power) winding is grid-connected, and the secondary (control) winding is normally supplied from a bi-directional power converter. A BDFG reluctance type (Fig. 1), the brushless doubly-fed reluctance generator (BD-FRG) [1]–[4], appears to be more attractive than its 'nested' cage rotor form, the brushless doubly-fed induction generator (BDFIG) [5]–[7], [11], [12]. This preference has been mainly attributed to the prospect for higher efficiency [2] and simpler control[1] associated with the cage-less reluctance rotor [14]. However, the BDFG rotor must have half the total number of stator poles to provide the rotor position dependent magnetic coupling between the stator windings required for the machine torque production [3].

With the introduction of the grid codes [15], another important BDFG merit is the superior low-voltage-fault-ride-through (LVFRT) capability to the DFIG [16]–[18]. It has

The authors are with the Faculty of Engineering and Environment, Department of Physics and Electrical Engineering, Northumbria University Newcastle, Newcastle upon Tyne, United Kingdom. Email: sul.ademi@northumbria.ac.uk; milutin.jovanovic@northumbria.ac.uk; jude-kennedy.obichere@northumbria.ac.uk

[1]Field-oriented control of the primary reactive power and electromagnetic torque is inherently decoupled in both the BDFRG and DFIG [13], but not in the BDFIG [6], [12].
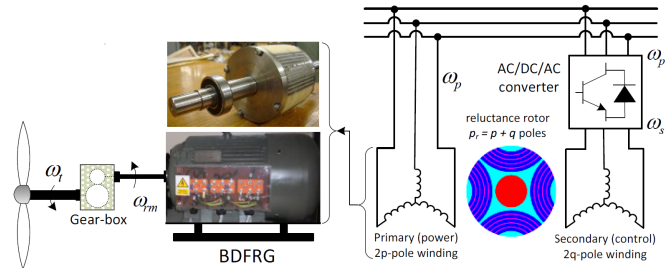

Fig. 1. A conceptual diagram of the variable speed WECS with BDFRG.

been shown that owing to the larger leakage inductances and lower fault current levels, the LVFRT of the BDFIG may be accomplished safely without a crowbar circuitry [15], [19]. These potential LVFRT performance advantages over the DFIG can be carried over to the BDFRG featuring the leakage reactance values of the same order as the BDFIG.

Various control algorithms[2] have been developed for the BDFRG including scalar control [1], [21], vector control (VC) [1], [13], [21], direct torque control [21], [22], torque and reactive power control [23], direct power control [24], sliding mode power control [25], and even non-linear Lyapunov control theory [8]. Although a comparative analysis of some of these control methods has been partly made in [21] (and more detailed for the DFIG in [16], [20]), to the best knowledge of the authors, no similar study has been reported specifically on Field-Oriented Control (FOC) vs VC, and there has been no or very little published work on true FOC implementation of the BDFRG. The most likely reason is that the two terms have often been interchangeably used to indicate the same control approach despite their quite distinctive meanings. In the BDFRG case, the 'FOC/VC' are commonly referred to as the primary winding flux/voltage oriented control respectively, by analogy to the stator flux/voltage oriented control of the DFIG. With a proper selection of the reference frames, the two control techniques become very similar in nature and dynamic response, especially with larger machines of lower resistances. Nevertheless, they have clear differences and performance trade-offs to be pointed out in this paper using the maximum torque per inverter ampere (MTPIA) strategy [1], [26] on a custom-designed 2 MW BDFRG [4]. This control objective has been considered because of the achievable efficiency gain by reducing both the secondary winding copper and inverter switching losses [1]. Extensive realistic simulation results taking into account the usual practical effects (e.g. transducers' DC offset, noise in measurements, and a PWM power converter model) are presented to support the discussions.

[2]A good literature review on control of the BDFIG can be found in [5]–[7], and of the DFIG in [16], [20].

II. MODELING AND OPERATING PRINCIPLES

The BDFRM(G) dynamic model in arbitrary rotating reference frames, using standard notation and assuming motoring convention, can be represented as [3]:

$$
\left.
\begin{aligned}
\underline{v}_p &= R_p \underline{i}_p + \frac{d\underline{\lambda}_p}{dt} = R_p \underline{i}_p + \frac{d\underline{\lambda}_p}{dt}\bigg|_{\theta_p \, const} + j\omega_p \underline{\lambda}_p \\
\underline{v}_s &= R_s \underline{i}_s + \frac{d\underline{\lambda}_s}{dt} = R_s \underline{i}_s + \frac{d\underline{\lambda}_s}{dt}\bigg|_{\theta_s \, const} + j\omega_s \underline{\lambda}_s \\[4pt]
\underline{\lambda}_p &= \underbrace{L_p i_{pd} + L_{ps} i_{sd}}_{\lambda_{pd}} + j \cdot \underbrace{(L_p i_{pq} - L_{ps} i_{sq})}_{\lambda_{pq}} \\
\underline{\lambda}_s &= \lambda_{sd} + j \cdot \lambda_{sq} = \sigma L_s \underline{i}_s + \underbrace{\frac{L_{ps}}{L_p} \underline{\lambda}_p^*}_{\lambda_{ps}}
\end{aligned}
\right\} \quad (1)
$$

where the primary and secondary winding are denoted by the subscripts 'p' and 's' respectively, $\sigma = 1 - L^2{}_{ps}/(L_p L_s)$ is the leakage factor, and λ_{ps} is the primary flux linking the secondary winding (i.e. the mutual flux linkage).

The fundamental angular velocity and torque relationships for the machine with p_r rotor poles and $\omega_{p,s} = 2\pi f_{p,s}$ applied frequencies to the respective $2p$-pole and $2q$-pole windings (Fig. 1) are [3]:

$$
\omega_{rm} = \frac{\omega_p + \omega_s}{p_r} \iff n_{rm} = 60 \cdot \frac{f_p + f_s}{p_r} \quad (2)
$$

$$
T_e = \frac{3p_r}{2}(\lambda_{ps_d} i_{sq} - \lambda_{ps_q} i_{sd}) \quad (3)
$$

$$
T_a = J \cdot \frac{d\omega_{rm}}{dt} = T_e - T_L(\omega_{rm}) - F \cdot \omega_{rm} \quad (4)
$$

Notice that $\omega_s > 0$ for 'super-synchronous' operation, and $\omega_s < 0$ at 'sub-synchronous' speeds (i.e. an opposite phase sequence of the secondary to the primary winding) in (2) where $\omega_{syn} = \omega_p/p_r$ is the synchronous speed (for $\omega_s = 0$ i.e. a DC secondary) as with a $2p_r$-pole wound rotor synchronous turbo-machine. It is also worth mentioning that all the ω_p rotating vectors in the primary voltage/flux equations in (1) are in ω_p frame, while the corresponding secondary counterparts, including the λ_{ps} components in (3), are stationary in $p_r\omega_{rm} - \omega_p = \omega_s$ frame [3]. Given that λ_p and λ_{ps} in (3) are approximately constant by the primary winding grid connection, torque control can obviously be achieved through the secondary dq currents in the ω_s frame.

Using (2), one can derive the mechanical power equation showing individual contributions of each BDFRG winding:

$$
P_m = T_e \cdot \omega_{rm} = \underbrace{\frac{T_e \cdot \omega_p}{p_r}}_{P_p} + \underbrace{\frac{T_e \cdot \omega_s}{p_r}}_{P_s} = P_p \cdot \left(1 + \frac{\omega_s}{\omega_p}\right) \quad (5)
$$

The machine operating mode is determined by the power flow in the primary winding i.e. to the grid for the generating ($T_e < 0$) regime under consideration, while the secondary winding can either take or deliver real power (P_s) subject to its phase sequence i.e. the ω_s sign; the BDFRG would absorb (produce) $P_s > 0$ at sub (super)-synchronous speeds.

III. CONTROLLER CONFIGURATION

A structural diagram of the primary voltage/flux angle and frequency estimation technique in discrete form with appropriate dq frame alignment options for VC/FOC blocks is shown in Fig. 2. The entire BDFRG system layout with
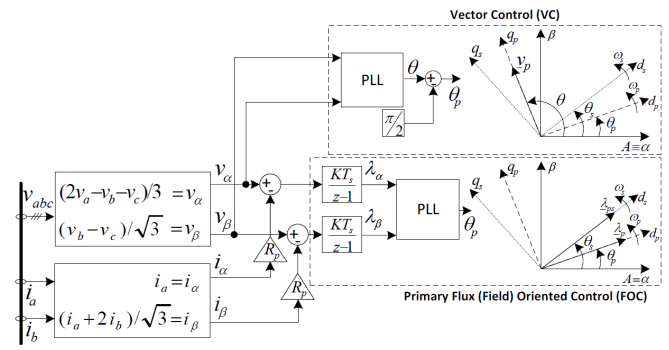

Fig. 2.   Identification of primary voltage and flux vectors in a stationary $\alpha - \beta$ frame.
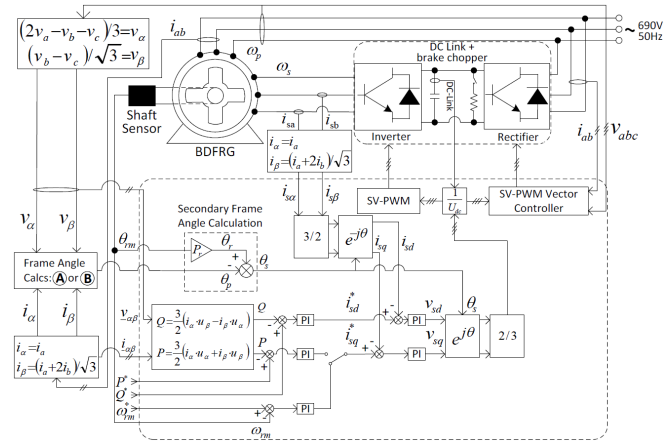

Fig. 3.   Structure of a BDFRG drive setup.

a generic controller design is presented Fig. 3. A standard phase-locked-loop (PLL) algorithm, readily available in the $Simulink$ library, has been used to retrieve the stationary $\alpha - \beta$ frame angular positions (θ/θ_p) of the primary voltage/flux vectors from the measured voltages and/or currents. Furthermore, a conventional vector controller with space-vector PWM of the active rectifier has been implemented for control of DC link voltage and unity line power factor [27]. The primary real (P) and reactive (Q) power calculations are reference frame invariant and have been done using the stationary frame voltages ($v_{\alpha\beta}$) and currents ($i_{\alpha\beta}$) to avoid unnecessary conversions into their rotating $d_s - q_s$ equivalents and the use of time-consuming trigonometric functions allowing so the higher control rates and superior performance in practice. The Q reference is often set to zero ($Q^* = 0$) for the unity primary power factor but can be any other value of interest for a given real power setting (P^*) in power control mode, or the desired angular velocity (ω_{rm}^*) in variable speed systems. For example, either P^* or ω_{rm}^* may correspond to the Maximum Power Point Tracking (MPPT) of a wind turbine [1], [8] while Q^* may be chosen to optimize certain performance indicator of the machine like torque per secondary ampere in this paper.

IV. VOLTAGE-ORIENTED CONTROL (VC)

The control form expressions can be derived from the BDFRG space-vector model (1) in the natural reference frames, ω_p (e.g. $d_p - q_p$ for primary winding) and ω_s (e.g. $d_s - q_s$ for secondary winding) rotating frames (Fig. 2),

where the respective vector components appear as DC quantities. Substituting for $\underline{i}_p$ from the $\underline{\lambda}_p$ equation of (1) into $\underline{S}_p = \frac{3}{2}\underline{v}_p i_p^*$ would lead to the following relationships for the primary mechanical and reactive power:

$$P_{p_{vc}} = \frac{3}{2}\omega_p(\lambda_{ps_d}i_{sq} - \lambda_{ps_q}i_{sd}) \qquad (6)$$

$$= P_{p_{foc}} - \frac{3}{2}\omega_p\lambda_{ps_q}i_{sd} \qquad (7)$$

$$Q_{p_{vc}} = \frac{3}{2}\omega_p\left(\frac{\lambda_p^2}{L_p} - \lambda_{ps_d}i_{sd} - \lambda_{ps_q}i_{sq}\right) \qquad (8)$$

$$= Q_{p_{foc}} - \frac{3}{2}\omega_p\lambda_{ps_q}i_{sq} \qquad (9)$$

VC of P_p and Q_p is coupled as both the i_{sd} and i_{sq} secondary current components appear in (6) and (8). The level of coupling can be reduced by aligning the q_p-axis of the reference frame to the primary voltage vector as proposed in Fig. 2. In this case, the primary flux vector ($\underline{\lambda}_p$) would be phase shifted ahead of the corresponding d_p-axis depending on the winding resistance values which are getting smaller with larger machines. Therefore, for the frame alignment as in Fig. 2, VC should be similar to FOC as $\lambda_{ps_d} >> \lambda_{ps_q}$ i.e. $\lambda_{ps_d} \approx \lambda_{ps}$ so that (6) and (8) become:

$$P_{p_{vc}} \approx P_{p_{foc}} = \frac{3}{2}\omega_p\lambda_{ps}i_{sq} = \frac{3}{2}\frac{L_{ps}}{L_p}\omega_p\lambda_p i_{sq} \qquad (10)$$

$$Q_{p_{vc}} \approx Q_{p_{foc}} = \frac{3}{2}\frac{\omega_p\lambda_p^2}{L_p} - \frac{3}{2}\omega_p\lambda_{ps}i_{sd} \qquad (11)$$

$$= \frac{3}{2}\frac{\omega_p\lambda_p}{L_p}(\lambda_p - L_{ps}i_{sd}) = \frac{3}{2}\omega_p\lambda_p i_{pd} \qquad (12)$$

The P_p vs i_{sq} and Q_p vs i_{sd} functions above are nearly linear, which justifies the use of PI controllers in Fig. 3.

V. FLUX-ORIENTED CONTROL (FOC)

The primary flux oriented (e.g. with the reference frame d_p-axis aligned to $\underline{\lambda}_p$ as in Fig. 2) forms of the flux equations in (1) and (3) become [3], [13], [21]:

$$\underline{\lambda}_p = \underbrace{L_p i_{pd} + L_{ps}i_{sd}}_{\lambda_{pd}=\lambda_p} + j\cdot\underbrace{(L_p i_{pq} - L_{ps}i_{sq})}_{\lambda_{pq}=0} \qquad (13)$$

$$\underline{\lambda}_s = \underbrace{\sigma L_s i_{sd} + \lambda_{ps}}_{\lambda_{sd}} + j\cdot\underbrace{\sigma L_s i_{sq}}_{\lambda_{sq}} = \sigma L_s\underline{i}_s + \underbrace{\frac{L_{ps}}{L_p}\lambda_p}_{\lambda_{ps}} \qquad (14)$$

$$T_e = \frac{3p_r L_{ps}}{2L_p}\lambda_p i_{sq} = \frac{3p_r}{2}\lambda_{ps}i_{sq} = \frac{3p_r}{2}\lambda_p i_{pq} \qquad (15)$$

The corresponding real and reactive power are now given by (10) and (12).

The most important advantage of FOC over VC is the inherently decoupled control of P_p (or T_e) and Q_p through i_{sq} and i_{sd} variations, respectively, which is immediately obvious from (10), (12) and (15). This fact greatly facilitates the FOC design. In favor of VC, it is fair to say that these appealing FOC properties come at the cost of the $\underline{\lambda}_p$ angle estimation (θ_p in Ⓑ block of Fig. 2) and difficulties with suppressing the detrimental DC offset effects on the voltage integration accuracy. In addition, the primary winding resistance (R_p) generally needs to be known, and especially with decreasing machine sizes. As entirely parameter independent, the VC approach does not suffer from any of these FOC

TABLE I
THE BDFRG DESIGN SPECIFICATIONS

Rotor inertia [J]	3.8 kgm^2
Primary resistance [R_p]	0.0375 Ω
Secondary resistance [R_s]	0.0575 Ω
Primary inductance [L_p]	1.17 mH
Secondary inductance [L_s]	2.89 mH
Mutual inductance [L_{ps}]	0.98 mH
Rotor poles [p_r]	4
Primary power [P_r]	2 MW
Rated speed [n_r]	1000 rev/min
Stator currents [$I_{p,s}$]	1.5 kA rms
Primary voltage [V_p]	690 V rms
Supply frequency [f_p]	50 Hz
Winding connections	Y/Y
Stator poles [p/q]	6/2

constraints but has compromised load disturbance rejection abilities and inferior control quality as a trade-off.

VI. MTPIA OPERATION OF BDFRG WIND TURBINE

The preliminary performance comparisons of the FOC/VC schemes in Fig. 3 have been carried out using the parameters of a large-scale custom-designed BDFRG [4] summarized in Table I. In order to make the simulations as realistic as possible, the following actions have been taken and/or assumptions made: (i) The power electronic models from the $SimPowerSystems$ toolbox have been implemented; (ii) High-frequency uncorrelated white noise and unknown slowly varying DC offset have been superimposed to the ideal signals to account for practical effects of the measurement noise and current/voltage transducers errors; (iii) Finally, the rotor position and speed information has been provided by a shaft sensor.

In a typical wind energy conversion system, the turbine output torque on the generator side of the gear-box for the maximum energy extraction from the wind in the base speed region (i.e. between the minimum 'cut-in', $u_{\min}$, and the rated wind speed, u_r), can be represented as [1], [8]:

$$T_{opt} = \frac{A\cdot\rho\cdot C_p(\lambda_{opt},\gamma)\cdot R^3}{2\cdot g^3\cdot\lambda_{opt}^3}\cdot\omega_{rm}^2 = K_{opt}\cdot\omega_{rm}^2 \quad (16)$$

where ρ is the air density, $C_p(\lambda,\gamma)$ is the power (performance) coefficient (i.e. the maximum turbine efficiency as $\lambda = \lambda_{opt}$ in this case), $\lambda_{opt} = R\omega_t/u$ is the optimum tip speed ratio for a given wind speed u, ω_t is the turbine rotor angular velocity, γ is the pitch angle (normally fixed to zero to maximise C_p), R the radius of the circular swept area ($A = \pi R^2$), and $g = \omega_{rm}/\omega_t$ is the gear ratio. The shaft torque-speed profile in (4) is of the same form as (16):

$$T_L = -\frac{P_r}{\omega_r}\cdot\left(\frac{n_{rm}}{n_{\max}}\right)^2 \approx -19\cdot\left(\frac{n_{rm}}{1000}\right)^2\text{kNm} \quad (17)$$

The simulation results in Figs. 4-6 have been produced by running the control algorithms in Fig. 3 in speed mode at 5 kHz switching rate for the IGBT converter. The DC link voltage has been maintained at ≈ 1200 V by the PWM rectifier (i.e. the line-side bridge) supplied at 690 V, 50 Hz. The reference speed trajectory is set as a steep ramp signal suited for dynamically not very demanding wind power applications even under extreme turbulent wind conditions.
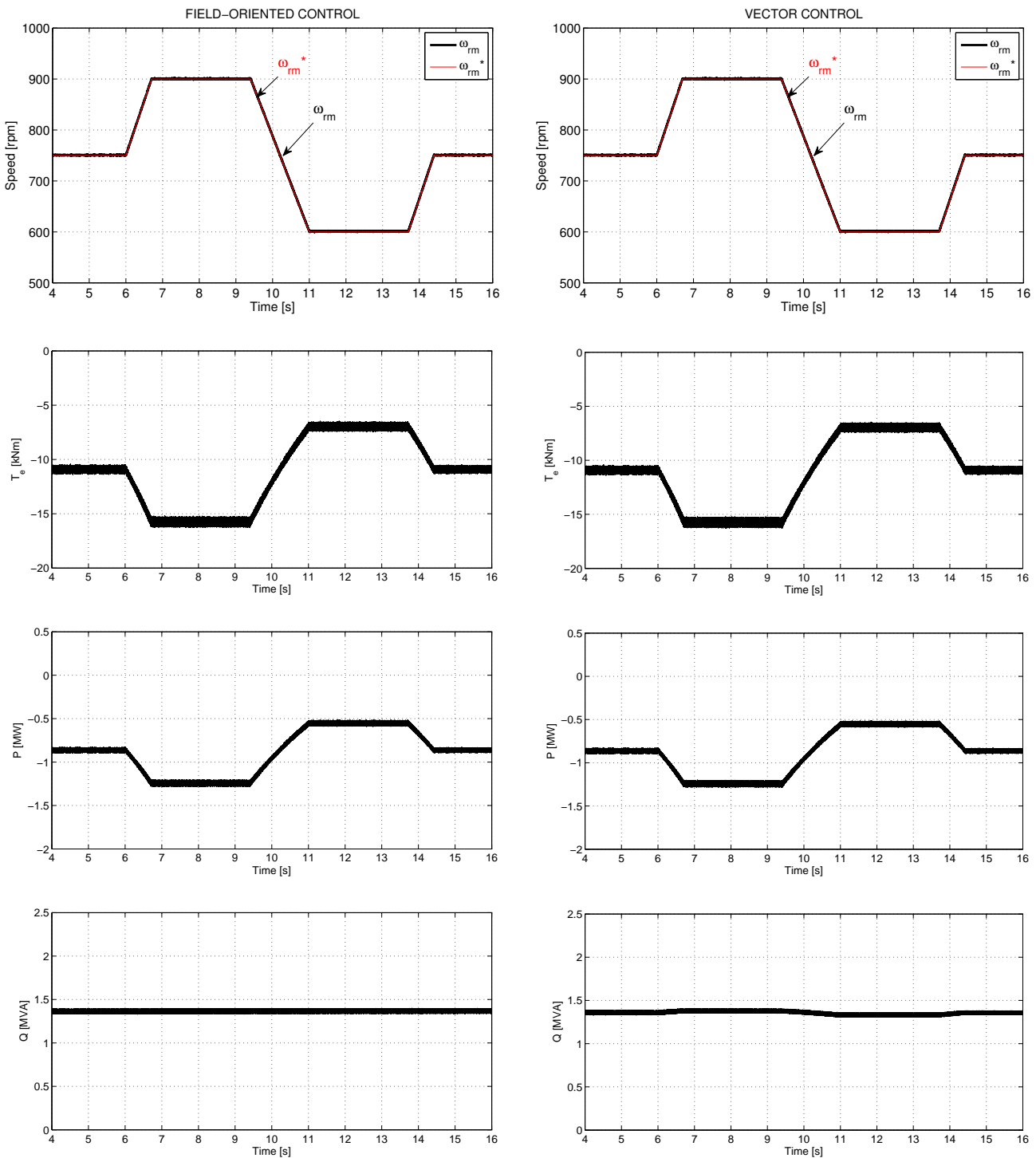
Fig. 4. MTPIA performance of the BDFRG in a narrow range around synchronous speed (750 rev/min).

The top plots in Fig. 4 show the excellent speed tracking with no overshoot following the start-up period of the BDFRG. Note that the speed response is virtually identical for the FOC and VC. The primary electrical power (P) and electro-magnetic torque (T_e) curves reflect (17) for the specific speed settings. Except for a difference in losses, and considering that $\omega_p \approx const$, P and T_e are directly related as follows from (5) and (6) which explains a close resemblance in their shape. The T_e deviations from the desired load profile during the speed transients refer to the acceleration or deceleration torque term in (4) depending on whether the

machine is to speed-up ($T_a > 0$) or slow-down ($T_a < 0$). One can also hardly see any disparity between the FOC and VC results under the MTPIA conditions ($i_{sd} = 0$) when (6) effectively becomes (10).

The reactive power (Q) is controlled at ≈ 1.35 MVAr, obtained from (12) for $i_{sd} = 0$ and $\lambda_p \approx u_p/\omega_p$, to minimize the i_s magnitude for a given shaft torque and meet the MTPIA objective. Note that the Q behavior with the decoupled FOC is largely unaffected by the P variations. The VC waveform, however, is rather distorted due to the presence of the coupling i_{sq} term in (8).
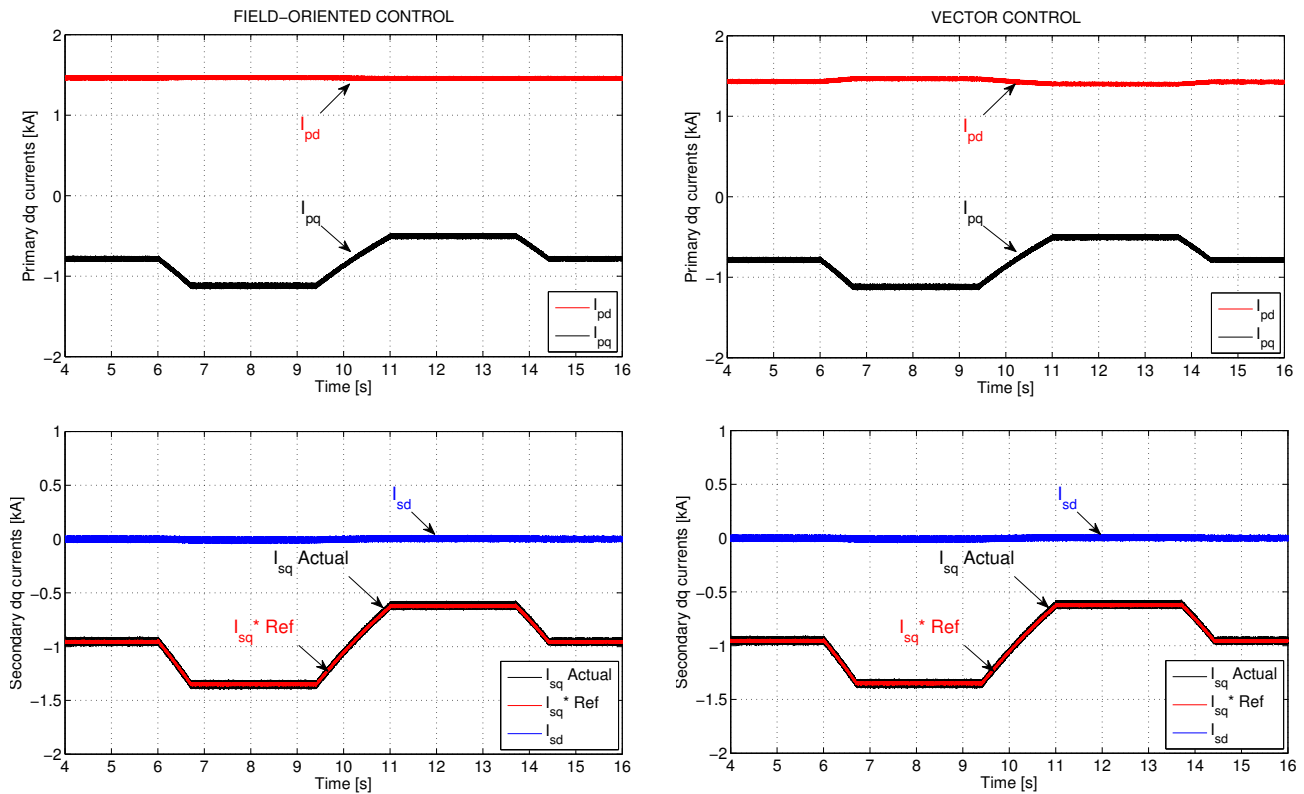
Fig. 5.   MTPIA responses of the BDFRG current components in the corresponding rotating reference frames.
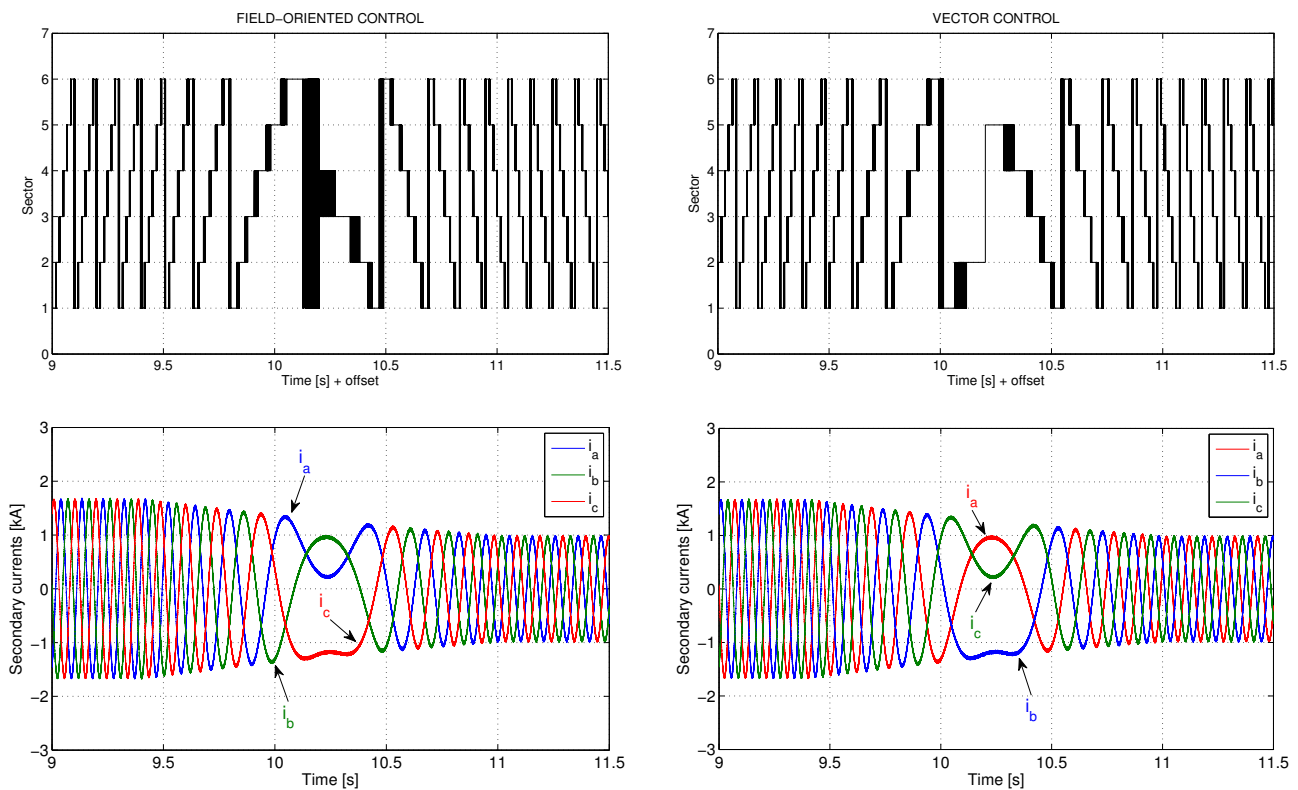

Fig. 6.   BDFRG inferred secondary voltage positions and secondary current waveforms showing a phase sequence reversal during the transition from super- to sub-synchronous speed mode.

The secondary ($i_{sd,q}$) and primary ($i_{pd,q}$) current waveforms in Fig. 5 are notably smooth with no transient over-currents as the PI regulators do not need to be saturated to allow accurate tracking of the desired trajectories for the moderate trapezoidal speed variations. A close link between the active q currents and the real power (torque), as well as the magnetizing d currents and Q, is immediately visible from the respective waveforms. The coupling effects of the i_{sq} clearly manifest themselves as speed (torque) dependent disturbance (e.g. offsets) in the respective non-controllable i_{pd} profiles by analogy to the P and Q scenario in the VC case. The FOC i_{pd} (and Q) levels, on the other hand, are constant in average sense throughout.

Fig. 6 shows the step-wise PWM sector change of the modulated secondary voltage vector ($\underline{v}_s$), and the respective current variations, during a speed reduction from 900 rev/min to 600 rev/min. In the super-synchronous mode, $\underline{v}_s$ rotates anti-clockwise as indicated by the ascending sector numbers for the same phase sequence of the windings and $\omega_s > 0$ in (2). The situation is reversed at sub-synchronous speeds when $\underline{v}_s$ rotates clockwise with the sector numbers descending, which comes from the opposite phase sequence of the secondary to the primary winding since $\omega_s < 0$ in (2). Notice that $\underline{v}_s$ becomes stationary at synchronous speed as the secondary currents are then DC i.e. $\omega_s = 0$ in (2).

VII. Conclusions

The main contribution of the work is the comparative development and performance analysis of field (primary flux) oriented control (FOC) and vector (primary voltage oriented) control (VC) algorithms for optimum operation of the BDFRG - a viable, low cost and reliable alternative to its widely-used companion, the conventional slip-ring doubly-fed induction generator (DFIG). This control framework can serve as a basis for further research on this emerging brushless machine topology for applications with limited variable speed ranges, foremost wind turbines (but also centrifugal pump-alike drives), where the cost advantages of partially-rated power electronics and high reliability of brushless structure can be fully exploited. The realistic simulation studies have clearly demonstrated the undoubt potential and effectiveness of the controller(s) using the maximum torque per inverter ampere strategy. Such encouraging results warrant further practical investigation of both the machine itself and the dedicated control approaches being undertaken.

References

[1] M. G. Jovanovic, R. E. Betz, and J. Yu, "The use of doubly fed reluctance machines for large pumps and wind turbines," *IEEE Transactions on Industry Applications*, vol. 38, pp. 1508–1516, 2002.

[2] F.Wang, F.Zhang, and L.Xu, "Parameter and performance comparison of doubly-fed brushless machine with cage and reluctance rotors," *IEEE Transactions on Industry Applications*, vol. 38, no. 5, pp. 1237–1243, 2002.

[3] R. E. Betz and M. G. Jovanovic, "Introduction to the space vector modelling of the brushless doubly-fed reluctance machine," *Electric Power Components and Systems*, vol. 31, no. 8, pp. 729–755, 2003.

[4] D. G. Dorrell and M. Jovanović, "On the possibilities of using a brushless doubly-fed reluctance generator in a 2 MW wind turbine," *IEEE Industry Applications Society Annual Meeting*, pp. 1–8, Oct. 2008.

[5] R.A.McMahon, P.C.Roberts, X.Wang, and P.J.Tavner, "Performance of BDFM as generator and motor," *IEE Proc.-Electr. Power Appl.*, vol. 153, no. 2, pp. 289–299, March 2006.

[6] J. Poza, E. Oyarbide, I. Sarasola, and M. Rodriguez, "Vector control design and experimental evaluation for the brushless doubly fed machine," *IET Electric Power Applications*, vol. 3, no. 4, pp. 247–256, July 2009.

[7] K. Protsenko and D. Xu, "Modeling and control of brushless doubly-fed induction generators in wind energy applications," *IEEE Transactions on Power Electronics*, vol. 23, no. 3, pp. 1191–1197, May 2008.

[8] F. Valenciaga and P. F. Puleston, "Variable structure control of a wind energy conversion system based on a brushless doubly fed reluctance generator," *IEEE Transactions on Energy Conversion*, vol. 22, no. 2, pp. 499–506, June 2007.

[9] H. Polinder, F. van der Pijl, G. de Vilder, and P. Tavner, "Comparison of direct-drive and geared generator concepts for wind turbines," *IEEE Transactions on Energy Conversion*, vol. 21, no. 3, pp. 725–733, Sept. 2006.

[10] F. Spinato, P.J.Tavner, G. van Bussel, and E. Koutoulakos, "Reliability of wind turbine subassemblies," *IET Renewable Power Generation*, vol. 3, no. 4, pp. 387–401, Dec. 2009.

[11] S. Tohidi, M. Zolghadri, H. Oraee, P. Tavner, E. Abdi, and T. Logan, "Performance of the brushless doubly-fed machine under normal and fault conditions," *IET Electric Power Applications*, vol. 6, no. 9, pp. 621–627, Nov. 2012.

[12] F. Barati, R. McMahon, S. Shao, E. Abdi, and H. Oraee, "Generalized vector control for brushless doubly fed machines with nested-loop rotor," *IEEE Transactions on Industrial Electronics*, vol. 60, no. 6, pp. 2477–2485, June 2013.

[13] L. Xu, L. Zhen, and E. Kim, "Field-orientation control of a doubly excited brushless reluctance machine," *IEEE Transactions on Industry Applications*, vol. 34, no. 1, pp. 148–155, Jan/Feb 1998.

[14] A. Knight, R. Betz, and D. Dorrell, "Design and analysis of brushless doubly fed reluctance machines," *IEEE Transactions on Industry Applications*, vol. 49, no. 1, pp. 50–58, Jan/Feb 2013.

[15] T. Long, S. Shao, P. Malliband, E. Abdi, and R. McMahon, "Crowbarless fault ride-through of the brushless doubly fed induction generator in a wind turbine under symmetrical voltage dips," *IEEE Transactions on Industrial Electronics*, vol. 60, no. 7, pp. 2833–2841, 2013.

[16] R. Cardenas, R. Pena, S. Alepuz, and G. Asher, "Overview of control systems for the operation of DFIGs in wind energy applications," *IEEE Transactions on Industrial Electronics*, vol. 60, no. 7, pp. 2776–2798, 2013.

[17] G. Marques and D. Sousa, "Understanding the doubly fed induction generator during voltage dips," *IEEE Transactions on Energy Conversion*, vol. 27, no. 2, pp. 421–431, 2012.

[18] S. Tohidi, P. Tavner, R. McMahon, H. Oraee, M. Zolghadri, S. Shao, and E. Abdi, "Low voltage ride-through of DFIG and brushless DFIG: Similarities and differences," *Electric Power Systems Research*, vol. 110, no. 0, pp. 64–72, 2014.

[19] T. Long, S. Shao, E. Abdi, R. McMahon, and S. Liu, "Asymmetrical low-voltage ride through of brushless doubly fed induction generators for the wind power generation," *IEEE Transactions on Energy Conversion*, vol. 28, no. 3, pp. 502–511, 2013.

[20] E. Tremblay, S. Atayde, and A. Chandra, "Comparative study of control strategies for the doubly fed induction generator in wind energy conversion systems: A DSP-based implementation approach," *IEEE Transactions on Sustainable Energy*, vol. 2, no. 3, pp. 288–299, 2011.

[21] M. Jovanovic, "Sensored and sensorless speed control methods for brushless doubly fed reluctance motors," *IET Electric Power Applications*, vol. 3, no. 6, pp. 503–513, 2009.

[22] M. G. Jovanović, J. Yu, and E. Levi, "Encoderless direct torque controller for limited speed range applications of brushless doubly fed reluctance motors," *IEEE Transactions on Industry Applications*, vol. 42, no. 3, pp. 712–722, 2006.

[23] H. Chaal and M. Jovanović, "Practical implementation of sensorless torque and reactive power control of doubly fed machines," *IEEE Transactions on Industrial Electronics*, vol. 59, no. 6, pp. 2645–2653, 2012.

[24] H. Chaal and M. Jovanovic, "Power control of brushless doubly-fed reluctance drive and generator systems," *Renewable Energy*, vol. 37, no. 1, pp. 419–425, 2012.

[25] F. Valenciaga, "Second order sliding power control for a variable speed-constant frequency energy conversion system," *Energy Conversion and Management*, vol. 52, no. 12, pp. 3000–3008, 2010.

[26] R. E. Betz and M. G. Jovanovic, "Theoretical analysis of control properties for the brushless doubly fed reluctance machine," *IEEE Transactions on Energy Conversion*, vol. 17, pp. 332–339, 2002.

[27] M. Malinowski, M. Kazmierkowski, and A. Trzynadlowski, "A comparative study of control techniques for PWM rectifiers in ac adjustable speed drives," *IEEE Transactions on Power Electronics*, vol. 18, no. 6, pp. 1390–1396, 2003.